Elastic scattering of alpha particles from ^{209}Bi at 24.8, 28.5, 34.7, 38.8, and 69.5 MeV

P. Singh, A. Chatterjee, S. K. Gupta, and S. S. Kerekatte
Nuclear Physics Division, Bhabha Atomic Research Centre, Bombay 400 085, India
(Received 15 June 1990)

Differential cross sections for the elastic scattering of alpha particles from ^{209}Bi have been measured over a wide angular range at a number of energies between 24 and 70 MeV. The present data along with existing data in this energy range have been analyzed using the optical model with both phenomenological and double-folded potentials. The application of the dispersion relation of Mahaux, Ngô, and Satchler allows a reproduction of the observed energy dependence of the real part of the potential. A nearside-farside decomposition of the data clearly reveals large-angle Fraunhöfer oscillations. The inelastic cross sections at 69.5 MeV have also been measured and the deformation lengths obtained from a distorted-wave Born analysis are consistent with values reported in the literature.

I. INTRODUCTION

For a long time, alpha-particle scattering has been known to be an important and well-established tool for studies of the general mechanism of reactions between complex nuclear particles and for exploring interesting nuclear structure properties. The α particle, being composite, in principle interacts with nuclei in a more complicated way than nucleons do. However, its attenuation in nuclear matter restricts the interaction to the low-density surface region of the nucleus, particularly if the bombarding energy is not too high. In addition, the fact that the α particle has high binding energy, zero spin, and zero isospin may lead to a relatively uncomplicated interpretation of its interaction with nuclear matter, resulting in information on nucleon densities.

During the past several decades, a vast amount of data for elastic scattering of α particles has been collected.[1,2] Most of these data have been analyzed in terms of the optical model in which the interaction between the α particle and the nucleus is represented by a complex potential. In these analyses, both phenomenological potentials (usually of the Saxon-Woods type) as well as those obtained from microscopic calculations have been used.

Analyses of low-energy data with Saxon-Woods potentials suffer from discrete and continuous ambiguities[3] in the determination of the potential parameters. Most apparent are the ambiguities in the depth of the real potential, and it has been suggested that only its strength at the strong absorption radius can be determined uniquely. The ambiguity problems are, however, reduced at higher energies. Therefore, at lower energies one can start with parameters consistent with those at higher energies, following the energy dependence established from the systematics.[4]

In this paper we report on elastic-scattering studies of α particles from ^{209}Bi carried out to reduce the ambiguities in the optical-model parameters. In Sec. II the experimental details are given. Section III deals with the analysis of the data. In Sec. IV our results are summarized.

II. EXPERIMENTAL DETAILS

The experiments were performed with the unanalyzed α-particle beam at the Variable Energy Cyclotron Centre, Calcutta. The beam was focused to a spot of $\sim$3 mm diameter at the center of the 90-cm-diam scattering chamber. The beam energy spread was about $\pm$250 keV. The setup used in the present experiment was similar to that described in Ref. 5. The beam current ranged between 10 and 300 nA. Targets in the form of self-supporting foils of natural bismuth metal were prepared using the vacuum evaporation technique. The target thicknesses were determined by energy-loss measurements with an ^{241}Am α source. With the stopping power values tabulated by Northcliffe and Schilling,[6] the mean thicknesses of the two targets used were determined to be 0.65 and 2.97 mg/cm^2. Five 2-mm-thick surface-barrier detectors mounted 10° apart and subtending solid angles of 0.115, 0.208, 0.602, 0.604, and 0.736 msr were used. A 5-mg/cm^2-thick aluminum foil was mounted in front of

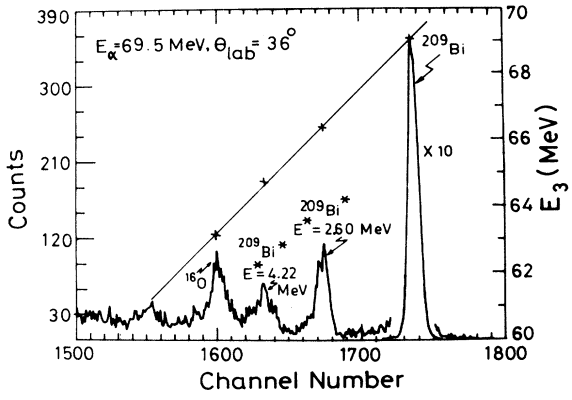

FIG. 1. Typical pulse-height spectrum at 69.5 MeV.

the detectors in order to stop fission fragments. The determination of the beam energy and the angular offset of the detectors was done using a simple method based on kinematics.[7] The offsets determined were less than 0.2°. The angles were corrected for the offsets. The angular distributions were measured in 1° steps for lower energies and in 2° steps at 69.5 MeV. The thicker target and higher beam currents were used for the measurements at backward angles. A typical pulse-height spectrum at 69.5 MeV is shown in Fig. 1. The elastic-scattering data at 24.8, 28.5, 34.7, 38.8, and 69.5 MeV, normalized by Rutherford cross sections, are shown in Fig. 2. The angular distributions for the inelastic scattering from the states at $E^*=2.60$ and 4.22 MeV are shown in Fig. 3.

III. ANALYSIS

The data have been analyzed using the optical model. Both phenomenological and folding model potentials have been employed in fitting the data with the optical model.

A. Phenomenological analysis

The elastic-scattering cross sections were analyzed using the standard phenomenological optical model, which for α particles takes the form

$$V(r)=V_C(r,r_C)-V_R f_R(r,r_R,a_R) - iW_I f_I(r,r_I,a_I)\ . \quad (1)$$

Here V_R and W_I are the strengths of the real and imaginary potentials, respectively, and the Saxon-Woods form factors are given by

$$f(r,r_x,a_x)=1/\{1+\exp[(r-R_x)/a_x]\}, \quad (2)$$

where $R_x=r_x A_T^{1/3}$, A_T being the target mass. The Coulomb potential $V_C(r,r_C)$ was taken as that due to a uniformly charged sphere of radius $R_C=r_C A_T^{1/3}$ with r_C fixed at 1.3 fm.

The data were fitted using the optical-model code SNOOPY8Q.[8] At these energies the ambiguities in the optical potential are particularly acute and cause difficulties in obtaining meaningful sets of optical potentials. We have followed the procedure of extrapolating to lower energies the "unique" real potential parameters determined

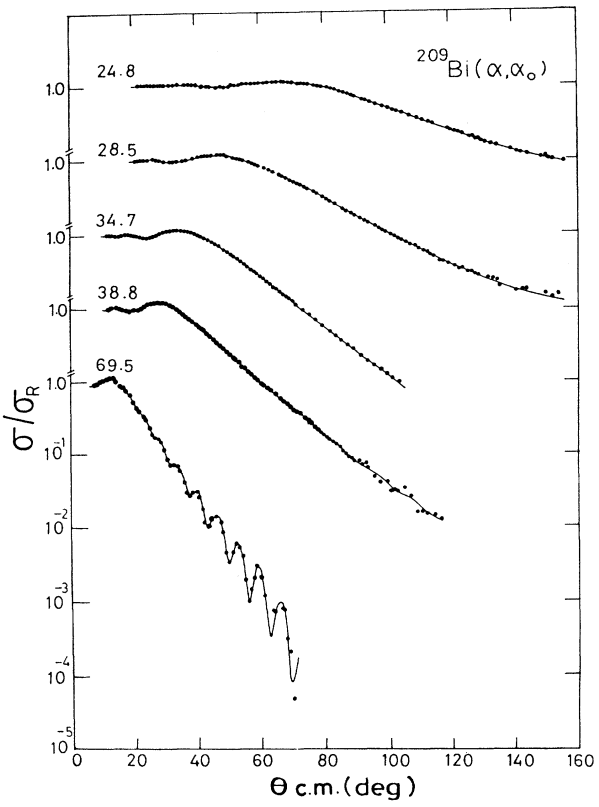

FIG. 2. Ratio of the elastic-scattering cross sections to the Rutherford cross sections plotted as a function of the center-of-mass angle for $E_\alpha=24.8$, 28.5, 34.7, 38.8, and 69.5 MeV. The solid lines are optical-model fits to the data using phenomenological potentials with the best-fit parameters given in Table II.

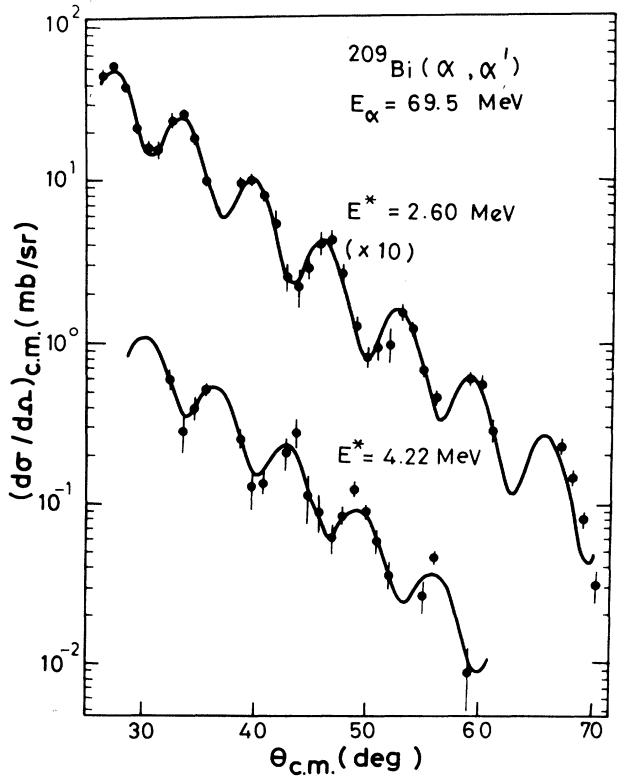

FIG. 3. Cross sections for the inelastic scattering to the states at $E^*=2.60$ and 4.22 MeV plotted as a function of the center-of-mass angle. The solid lines are calculated using the DWBA formalism assuming $l=2$ (4) at $E^*=2.60$ (4.22) MeV.

TABLE I. Optical-model parameters predicted from the systematics.

E (MeV)	V_R (MeV)	r_R (fm)	a_R (fm)	W_I (MeV)	r_I (fm)	a_I (fm)
22.0	106.90	1.362	0.621	12.30	1.409	0.642
24.8	107.01	1.360	0.624	13.27	1.412	0.648
28.5	107.16	1.357	0.627	14.44	1.415	0.654
34.7	107.24	1.354	0.633	16.01	1.422	0.665
38.8	107.56	1.351	0.637	16.91	1.425	0.672
42.0	107.69	1.348	0.641	17.57	1.426	0.678
50.5	108.00	1.343	0.649	18.92	1.436	0.724
69.5	108.67	1.329	0.670	20.96	1.436	0.781
104.0	109.78	1.302	0.710	22.88	1.437	0.781

at higher energies with a suitable energy variation.[5] For doing this effectively, we have made use of the systematics[4] of the volume integral J_R, the radius $R_{2.4}$, where the potential becomes 2.4 MeV, and the slope S of the potential at $R_{2.4}$ for the real potential. For the imaginary part of the potential, we have used the systematics[5] of the volume integral J_I and the ratio of geometry parameters, $R_{IR}(=R_I/R_R=a_I/a_R)$. By this prescription the parameters for the $\alpha+^{209}$Bi system at the energies of the measurements were predicted (Table I), and these are consistent with the ones determined at higher energies. Starting with these parameters, we have optimized the fits to the data by fine tuning the parameters to get the minimum χ^2 value. The final parameters are listed in Table II, and the fits to the data are shown in Fig. 2.

We have also reanalyzed the 22-MeV data of Barnett and Lilley,[9] the 42-MeV data of Alster,[10] and the 104-MeV data of Hauser *et al.*[11] In all cases we have fitted the data to the phenomenological optical model starting with the parameters predicted by the systematics,[4] and the resulting parameters are included in Table II. For the 22- and 104-MeV data, this procedure resulted in parameter sets completely different from those obtained in the original analysis[9,11] without any increase in the χ^2 values. For the 42-MeV data, the original analysis has been done only in terms of the parametrized phase-shift model of Austern and Blair.[12] The fits to the data at 22, 42, and 104 MeV are shown in Fig. 4.

It can be seen from Table II that the best-fit parameters obtained from our analyses at all energies, including the 22-, 42-, and 104-MeV data from the literature[9–11] are fairly close to the parameters predicted from the systematics. We have investigated the possible potential families which are allowed by the data. The χ^2 values are calculated for a range of J_R values with $R_{2.4}$, S, and the imaginary potential maintained at the best-fit values. The procedures for investigating the discrete potential family ambiguity is discussed in more detail in Ref. 5. A typical result, at 69.5 MeV, is shown in Fig. 5. In this figure the zeroth family corresponds to the best-fit parameters of Table II and the other families are indicated as $\pm1,\pm2,\ldots$. A similar analysis has been made for the imaginary part of the potential. In Fig. 6 we plot χ^2 as a function of J_I maintaining the $R_{2.4}$ and S of the imaginary part and real potential at the values corresponding to the best fit. In this case there is no family ambiguity.

TABLE II. Best-fit parameters from phenomenological analysis.

E (MeV)	V_R (MeV)	r_R (fm)	a_R (fm)	W_I (MeV)	r_I (fm)	a_I (fm)	χ^2/N	$J_R/4A$ (MeV fm^3)	$J_I/4A$ (MeV fm^3)	σ_R (mb)	Ref. for data
22.0	107.30	1.368	0.621	12.10	1.409	0.640	1.2	304	38	218	a
24.8	107.42	1.361	0.578	13.50	1.412	0.299	4.2	298	40	452	b
28.5	107.14	1.358	0.602	14.20	1.420	0.581	5.3	297	44	920	b
34.7	107.42	1.321	0.634	16.12	1.350	0.666	3.9	276	44	1323	b
38.8	107.51	1.374	0.635	16.88	1.478	0.600	3.4	310	60	1708	b
42.0	107.59	1.350	0.624	17.84	1.429	0.686	17.8	294	57	1811	c
50.5	108.20	1.356	0.641	16.00	1.454	0.790	2.4	300	56	2250	d
69.5	108.35	1.329	0.670	21.20	1.449	0.749	5.0	285	72	2583	b
104.0	109.80	1.278	0.710	18.57	1.464	0.781	1.0	261	66	2849	e

[a]Reference 9.
[b]Present measurement.
[c]Reference 10.
[d]Reference 5.
[e]Reference 11.

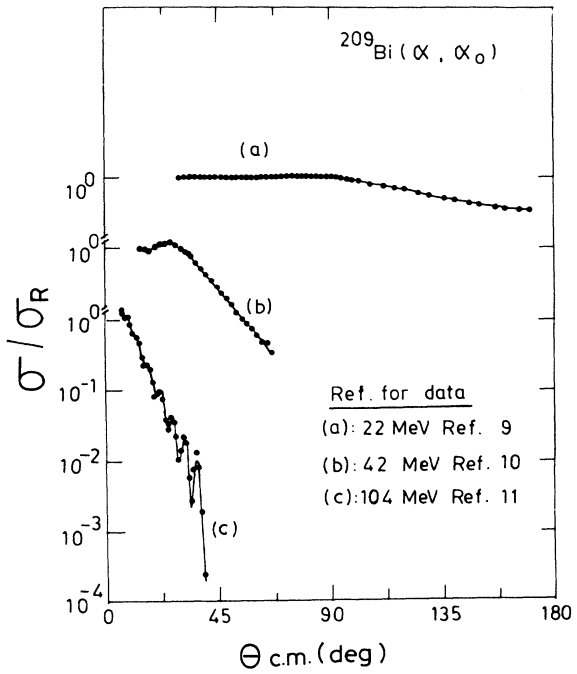

FIG. 4. Ratio of the elastic-scattering cross sections to the Rutherford cross sections plotted as a function of the center-of-mass angle for $E_\alpha = 22$, 42, and 104 MeV. The solid lines are the optical-model fit to the data using phenomenological potential with the best-fit parameter sets listed in Table II.

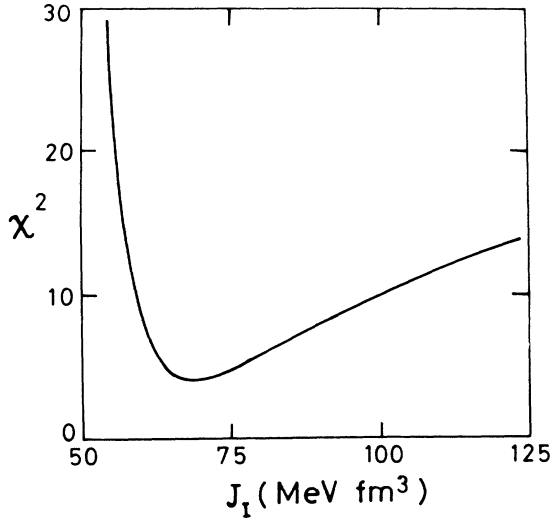

FIG. 6. Variation of the χ^2 per point as a function of the volume integral of the imaginary potential.

The reaction cross-section values (σ_R) are plotted as a function of energy in Fig. 7. The σ_R values at 22, 42, and 104 MeV (Refs. 9–11) are also included in the figure. It can be seen that there is a smooth behavior of σ_R over the whole energy domain.

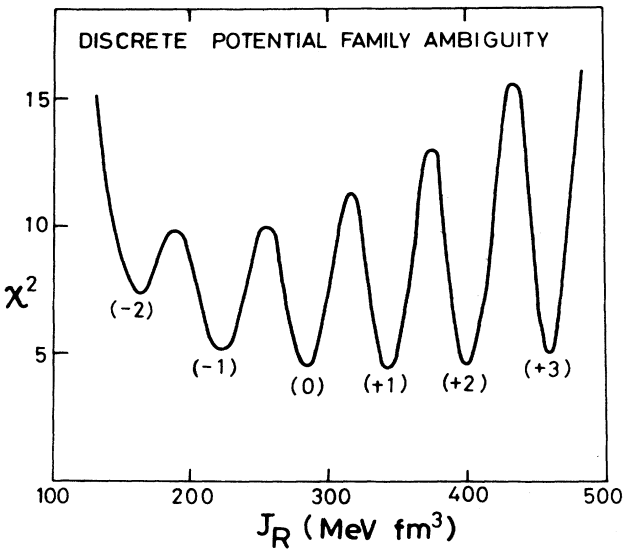

FIG. 5. Variation of the χ^2 per point as a function of the volume integral of the real potential. The labels (−2), (−1), (0), (+1), (+2), and (+3) represent different discrete potential families as discussed in the text.

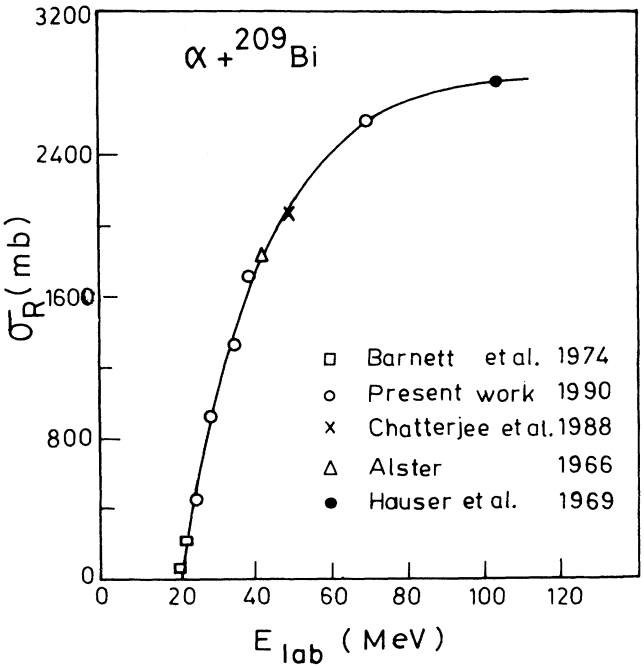

FIG. 7. Reaction cross section as a function of incident energy. The data points from the literature are also included. The solid line is drawn to guide the eye.

B. Microscopic analysis

The data were also analyzed using the folding model potential.[13] The double-folding potential for the system $\alpha+^{209}$Bi may be written as

$$U_F(\mathbf{r})=\int\int d\mathbf{r}_1 d\mathbf{r}_2 \rho_{\mathrm{Bi}}(\mathbf{r}_1)\rho_\alpha(\mathbf{r}_2)v(\mathbf{r}_{12}) , \quad (3)$$

where $\mathbf{r}$ is the separation of the centers of mass of the two colliding nuclei, v is the effective nucleon-nucleon interaction, and the ρ's are the point nucleon densities of the alpha particles and ^{209}Bi. The potentials were computed using the code DFPOT.[14] The interaction used was of the M3Y form,[13] given by

$$v(r)=7999e^{-4r}/4r-2134e^{-2.5r}/2.5r+J_{oo}\delta(r) , \quad (4)$$

where the third term accounts for knock-on exchange with $J_{oo}=-265$ MeV fm^3.

For the densities ρ_α and ρ_{Bi}, we used the charge-density distributions obtained by fitting the electron-scattering data and parametrized in the Fermi parabolic form[15]

$$\rho_p(r)=\rho_0(1+wr^2/c^2)/\{1+\exp[(r-c)/a]\} , \quad (5)$$

with $c=0.964$ fm, $a=0.322$ fm, $w=0.517$, and $\langle r\rangle^{1/2}=1.71$ fm for α particles, and $c=6.75$ fm, $a=0.468$ fm, $w=0$, and $\langle r\rangle^{1/2}=5.51$ fm for ^{209}Bi. The ρ_0 values were chosen so as to normalize the distributions to the charge numbers. The point nucleon densities were obtained from the charge densities after correcting for the finite size of the proton in the standard way.[13] In Fig. 8 the calculated microscopic potential is compared with the best-fit phenomenological potential for ^{209}Bi at $E_\alpha=28.5$ MeV. It can be seen that the two potential shapes are nearly the same around the strong absorption radius ($\sim$11 fm). A normalization of the microscopic potential by a factor of $\sim$1.7 brings it in closer agreement with the phenomenological potential. In carrying out the fits to the elastic-scattering data, the total potential used was

$$V(r)=-\lambda U_F(r)-iW_I(r)+V_C(r) . \quad (6)$$

In the analyses the folded real potential $U_F(r)$ was allowed an overall adjustable normalization coefficient λ. The forms of the imaginary potential $W_I(r)$ and the Coulomb potential $V_C(r)$ were same as that used in the phenomenological analyses of the data. The best fits were obtained by varying the parameters λ and $W_I(r)$. The parameters corresponding to best fits are listed in Table III.

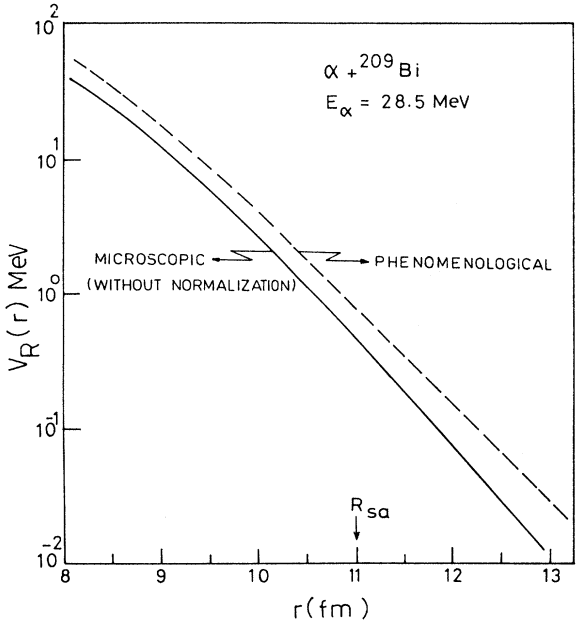

FIG. 8. Comparison of the real potentials $V_R(r)$ for $E_\alpha=28.5$ MeV obtained using phenomenological and microscopic prescriptions. The strong absorption radius R_{SA} has also been indicated.

The consistency between the real and imaginary parts of the optical potential can be tested by comparing with the predictions of the dispersion relation.[16] The dispersion relation predicts the real-part values starting with the imaginary-part values at the radius region of sensitivity as

$$\Delta V_{E_S}(r;E)=(E-E_S)\frac{P}{\pi}\int_0^\infty \frac{W(r;E')dE'}{(E'-E_S)(E'-E)} , \quad (7)$$

where P is the principal value of the integral, E_S is an adequate reference energy, and

$$\Delta V_{E_S}(r;E)=V(r;E)-V(r;E_S) . \quad (8)$$

TABLE III. Optical-model parameters from microscopic analysis.

E (MeV)	λ	W_I (MeV)	r_I (fm)	a_I (fm)	$J_I/4A$ (MeV fm^3)	χ^2/N	σ_R (mb)
22.0	2.28	20.62	1.330	0.570	53	1.0	215
24.8	1.40	20.62	1.360	0.365	56	4.3	453
28.5	1.67	20.40	1.376	0.552	58	6.7	919
34.7	1.71	25.13	1.390	0.471	73	6.9	1334
38.8	2.26	24.64	1.471	0.414	84	9.4	1615
42.0	1.90	21.37	1.491	0.395	75	11.7	1695
50.5	1.90	28.38	1.287	0.967	74	4.4	2307
69.5	1.61	29.67	1.297	0.990	79	8.0	2725
104.0	1.25	21.26	1.398	0.980	69	1.0	3044

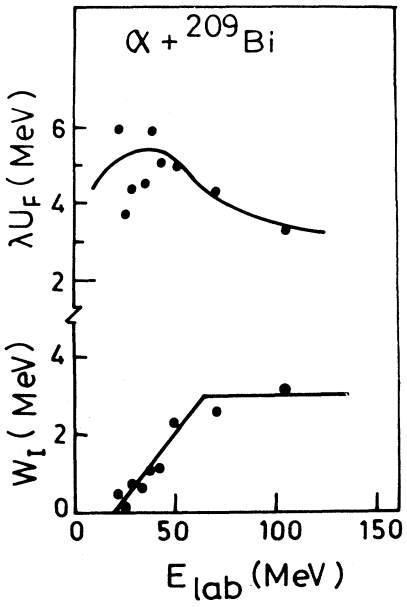

FIG. 9. Real and imaginary potential strengths at $r=10$ fm plotted as a function of the bombarding energy. The imaginary potential has been represented in the form of the two straight-line segments, and the resulting real potential calculated on the basis of the dispersion relation is shown as a continuous curve.

We have represented the imaginary potential values at $r=10$ fm by two straight-line segments[16] and computed the dispersive contribution to the real part. Figure 9 shows the results obtained taking a reference energy of 104 MeV and a comparison with the λU_F values of the microscopic potential. The dispersion relation gives a fair reproduction of the trend of the energy dependence of the real potential values obtained from the folding model analysis.

C. Notch perturbation test

A radial notch perturbation test has been carried out to determine the region of the potential most sensitive in predicting the elastic-scattering data. The procedure is to introduce a bipolar (volume integral conserving) radial perturbation in the potential into a localized radial region and to observe its effect on the predicted cross sections. In the present work we used the perturbed potential (for the real R and imaginary I parts)

$$V_p = V_{R(I)} f_{R(I)} \{1 - 10.4 D f_p(r)[1 - f_p(r)] \times [2 f_p(r) - 1]\} , \quad (9)$$

where

$$f_p(r) = 1/\{1 + \exp[(r - R_p)/a_p]\} . \quad (10)$$

The position of the center of this notch is the R_p parameter, and this can be varied over the whole radial region of the potential. In the present analysis, we have kept $a_p = 0.2$ and varied R_p from 5 to 14 fm, with the perturbation amplitude $D = 0.1$ for the real and imaginary parts separately and calculated the χ^2. In Fig. 10 the $\chi^2/\chi^2_{\min}$ values are plotted as a function of the notch radius R_p ($=R_{\text{notch}}$). It is seen that the potential is well determined in the region 8–11 fm. This region is inside the strong absorption radius (~ 11 fm). The ratio $\chi^2_{\max}/\chi^2_{\min}$ is much larger at higher energies for both the real and imaginary notch perturbation tests. This indicates that the potentials are better determined at higher energies. The angular distributions predicted by the perturbed potentials with notches at $r=8.5$ and 9.5 fm are compared with the calculations with the unperturbed potential in Fig. 11. It can be seen from the figure that the main angular region of sensitivity is for angles greater than 90°.

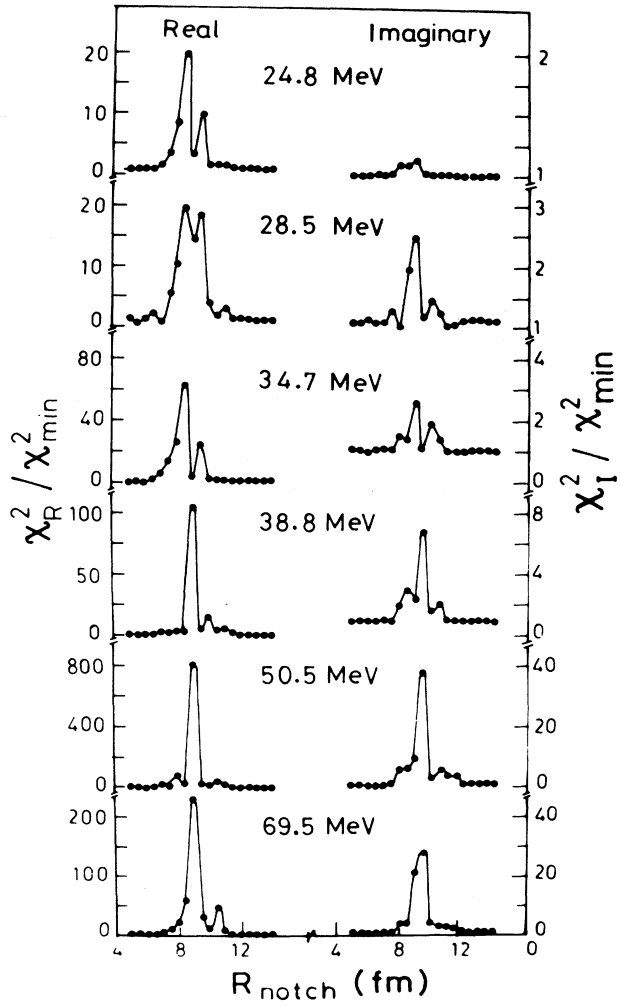

FIG. 10. Notch perturbation test $\chi^2/\chi^2_{\min}$ plotted as a function of the notch radius for the real and imaginary parts of the potentials. The solid lines are eye guide lines connecting the $\chi^2/\chi^2_{\min}$ values for different values of R_{notch} in steps of 0.5 fm for the real and imaginary parts, respectively.

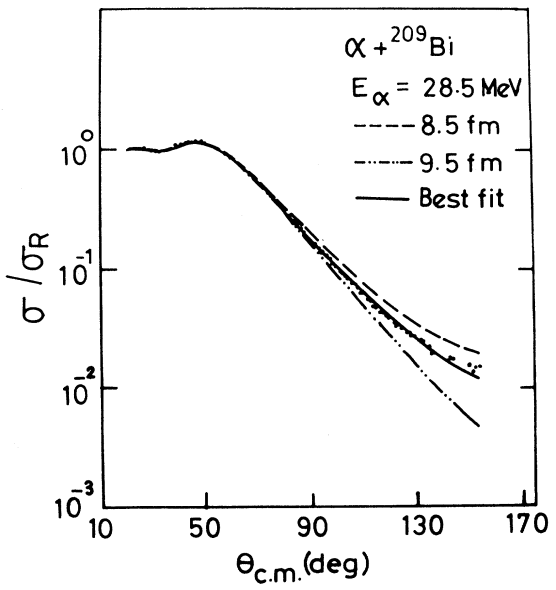

FIG. 11. Angular distribution predicted by the perturbed potentials having notches at $r=8.5$ fm (dashed line) and $r=9.5$ fm (dot-dashed line) are compared with the calculations using the unperturbed potential (solid line) at $E_\alpha=28.5$ MeV. Experimental data are also shown.

D. Nearside-farside decomposition

The angular distributions shown in Fig. 2 have a Fresnel diffraction pattern in the forward angular range and a Fraunhöfer pattern at the backward angles. A decomposition of the data into the farside and nearside components helps in filtering out the strong (but less sensitive to optical-model parameters) Fresnel part and enhances the relatively weak Fraunhöfer part. This technique[17,18] provides a good handle for getting at the reaction process taking place. In Fig. 12 we compare $\sigma/\sigma_{\text{near}}$ for the optical model and experimental cross sections at 69.5 MeV. It is seen that the oscillations which were less clearly seen in the σ/σ_R plot stand out rather prominently in the figure. The Fraunhöfer oscillations arise due to the interference of the near and far components. By presenting the data in this way, the quality of the fit to the data can be judged much better.

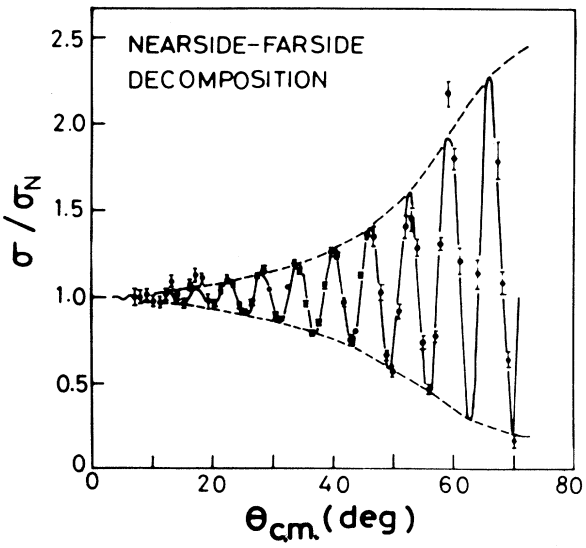

FIG. 12. Ratio of the experimental cross sections to the calculated nearside cross sections for 69.5 MeV plotted as a function of the center-of-mass angle and compared to the optical model predictions. The calculated values of $1\pm2(\sigma_F/\sigma_N)^{1/2}$ are drawn as envelopes.

E. Inelastic scattering

The inelastic-scattering cross sections to the states at excitation energies $E^*(^{209}\text{Bi})=2.60$ and 4.22 MeV have been obtained at the beam energy $E_\alpha=69.5$ MeV (Fig. 3). The cross sections of the 4.22-MeV state for $\theta_{\text{c.m.}}<32°$ could not be extracted due to the presence of ^{12}C and ^{16}O target contaminants. The yields from the other states were smaller and have not been included in the analyses.

The cross sections were analyzed in terms of the distorted-wave Born approximation (DWBA) model using the computer code DWUCK4.[19] In the calculations, the distorted waves used were those corresponding to the best-fit optical-model parameters for elastic scattering, and deformation parameters β_l were adjusted to fit the data. The results for the deformation lengths are

$$\beta_3 R\,(E^*\approx 2.60\text{ meV})=0.70\pm0.03\text{ fm},$$

$$\beta_4 R\,(E^*\approx 4.22\text{ MeV})=0.46\pm0.03\text{ fm}.$$

For the $E^*\approx2.60$ MeV, $l=3$ group of states, the previously reported deformation lengths are 0.75 ± 0.04 fm,[10] 0.71 ± 0.05 fm,[5] and 0.81 ± 0.03 fm.[20]

For the states clustered around $E^*\approx4.22$ MeV, the cross sections were best reproduced with a single l value ($l=4$). In high-resolution (p,p') studies,[21] the combined deformation lengths of levels ranging in E^* from 4.09 to 4.36 MeV are $\beta_2 R=0.28$ fm, $\beta_3 R=0.33$ fm, and $\beta_4 R=0.35$ fm. The present data also allow a DWBA fit to be made with $l=2$ (with a slightly poorer χ^2) resulting in $\beta_2 R=0.37\pm0.03$ fm; however, the data are not sensitive to the $l=3$ contribution in this E^* region due to the limited angular range of the measurement.

IV. SUMMARY AND CONCLUSION

Data have been presented for elastic scattering of α particles from ^{209}Bi at 24.8, 28.5, 34.7, 38.8, and 69.5 MeV. Optical-model analyses of these data were made and good fits were obtained. The starting values of the potential parameters were those predicted by extrapolating the parameters at higher energies using the systematics of J_R, $R_{2.4}$, and S for the real potential and J_I and R_{IR} for the imaginary potential. It was found that the final sets of parameters are not far removed from the starting ones, indicating that the global alpha-nucleus

systematics[5] are reasonable in predicting the parameters for the present system. Reanalysis of the data at 22, 42, and 104 MeV from the literature was performed starting with the parameters predicted from the systematics. The resulting potential parameters were again close to the starting ones. These parameter sets, although completely different from those in the original analyses, gave equally good fits to the data.

It is also reassuring to see that the λ value obtained in the microscopic analysis is similar to the normalization factor required to match the folding potential to the best-fit phenomenological potential around the strong absorption radius (Fig. 8).

The dispersion relation which links the real part of the potential to the imaginary part at a given radius was applied to calculate the dispersive contribution to the real part at the "sensitivity" radius. It was found that the general trend of the fitted renormalized potential is reproduced.

The notch perturbation test has revealed that the sensitive region of the potential is from 8 to 11 fm for essentially all energies between 25 and 70 MeV. This region is inside the strong absorption radius (~ 11 fm).

The deformation lengths (βR), deduced from a DWBA analysis of the inelastic data for 69.5 MeV using the parameters determined from the elastic-scattering analysis, are broadly consistent with those obtained from other measurements in the literature.

We thank the staff of the Variable Energy Cyclotron, Calcutta, for the operation of the accelerator, Shri C. V. Fernandes for his help in taking the data, and Dr. S. Kailas for many useful discussions during the analyses.

[1]P. P. Singh and P. Schwandt, Nukleonika **21**, 451 (1976); in *Proceedings of the 2nd Louvain Cracow Seminar on the Alpha-Nucleus Interaction,* edited by G. Gregoire and K. Gotowski (University of Louvain, Louvain-La-Neuve, Belgium, 1978).

[2]E. Galioli and P. E. Hodgson, Rep. Prog. Phys. **49**, 951 (1986).

[3]D. F. Jackson and C. G. Morgan, Phys. Rev. **175**, 1402 (1968).

[4]S. K. Gupta and K. H. N. Murthy, Z. Phys. A **307**, 187 (1982); A. Sridhar, N. Lingappa, S. K. Gupta, and S. Kailas, Phys. Rev. C **30**, 1760 (1984).

[5]A. Chatterjee, S. K. Gupta, S. Kailas, and S. S. Kerekatte, Phys. Rev. C **37**, 1420 (1988).

[6]L. C. Northcliffe and R. F. Schilling, Nucl. Data Tables A **7**, 233 (1970).

[7]A. Chatterjee, S. K. Gupta, S. Kailas, S. S. Kerekatte, and P. Singh, Nucl. Instrum. Methods A **292**, 30 (1990).

[8]P. Schwandt, SNOOPY8Q optical model code, Indiana University (unpublished).

[9]A. R. Barnett and J. S. Lilley, Phys. Rev. C **9**, 2010 (1974).

[10]J. Alster, Phys. Rev. **141**, 1138 (1966).

[11]G. Hauser, R. Lohken, H. Rebel, G. Schatz, G. W. Schweimer, and J. Specht, Nucl. Phys. **A128**, 81 (1969).

[12]N. Austern and J. S. Blair, Ann. Phys. (N.Y.) **33**, 15 (1965).

[13]G. R. Satchler and W. G. Love, Phys. Rep. **55**, 183 (1979).

[14]J. Cook, Comput. Phys. Commun. **25**, 125 (1982).

[15]H. De Vries, C. W. De Jager, and C. De Vries, At. Data Nucl. Data Tables **36**, 495 (1987).

[16]C. Mahaux, H. Ngô, and G. R. Satchler, Nucl. Phys. **A456**, 134 (1986).

[17]R. C. Fuller, Phys. Rev. C **12**, 1561 (1975).

[18]M. S. Hussein and K. W. McVoy, Prog. Part. Nucl. Phys. **12**, 103 (1984).

[19]P. D. Kunz, University of Colorado report, 1982 (unpublished).

[20]J. F. Ziegler and G. A. Peterson, Phys. Rev. **165**, 1337 (1968).

[21]W. T. Wagner, G. M. Crawley, and G. R. Hammerstein, Phys. Rev. C **11**, 486 (1975).